

Einfluss der Partikelgröße und des Brechungsindizes auf Kugellinsen Astigmatismus Particle Tracking Velocimetry

The influence of particle size and refractive index on Ball Lens astigmatism particle tracking velocimetry

Philipp Brockmann¹, Hamid Tabaei Kazerooni^{1,2}, Luca Brandt², Jeanette Hussong¹

¹ AG Lasermesstechnik der Mehrphasenströmungen,
Lehrstuhl für Hydraulische Strömungsmaschinen, Ruhr-
Universität Bochum, Universitätsstr. 150, 44801 Bochum

² SeRC and Linne FLOW Centre,
KTH Mechanics,
SE-100 44 Stockholm, Sweden

Astigmatismus-PTV, Partikeldynamik, Suspensionsströmungen
Astigmatism-PTV, particle dynamics, sheared suspension flows

Abstract

In this paper we investigate how particle characteristics affect the performance of Astigmatism Particle Tracking Velocimetry that is utilized in bright field mode with transparent particles. Hence, we refer to this measurement technique as Ball Lens Astigmatism Particle Tracking Velocimetry (BLAPTV). In BLAPTV particles act as ball lenses that generate a bright focal point. We investigated the influence of the refractive index of both liquid and particles as well as the particle diameter on its performance. We show that particles of the same size but different material can be distinguished in BLAPTV by their calibration curves. Furthermore, we elaborated an adapted calibration method that allows to determine out-of-plane particle positions, for calibration curves that intersect in the a_x - a_y -space by including the light intensity information of the focal point. This adapted calibration method appears to be very robust against outliers, leading to an increased accuracy and measurement volume depth. Furthermore, we observed that the shape of calibration curves may change along the z -position for larger measurement volume depths. We present an intrinsic calibration strategy to account for this effect and validate it for a plane channel flow.

1 Introduction

Astigmatism Particle Tracking Velocimetry (APTV) is a technique to measure the 3D motion of particles suspended in a fluid. Since it was introduced by Kao and Verkmann in 1994, it has been developed further in numerous works (Kao and Verkmann 1994, Chen et al. 2009, Cierpka et al. 2010, 2011). In APTV, astigmatism is used to code 2D particle images with an additional depth information, such that the 3D particle position can be reconstructed. Typically, a cylindrical lens is introduced into the system to create astigmatism. As a single camera approach, APTV is a useful tool especially in microfluidics where multi-camera approaches fail due to imaging constraints and calibration problems (Cierpka and Kähler 2012). Meanwhile, APTV has been applied to a wide range of fluidic problems in different length scales. An

example for a microfluidic application is the work of Ragan et al. 2006, who studied the motion of living kidney cells. With $0.2\mu\text{m}$ fluorescent polystyrene tracers, their measurement volume depth was $2.5\mu\text{m}$. In contrast, the work of Buchmann et al. 2014 deals with a more macroscopic problem. They measured the motion of $110\mu\text{m}$ particles in a supersonic, impinging jet flow, while their measurement volume depth covered $5100\mu\text{m}$. For a detailed report of the history of the method and its different fields of application, the reader is referred here to Cierpka and Kähler 2012. In most studies, APTV is applied to perform flow measurements with fluorescent particles, which are very small in comparison to the flow geometry and the field of view. Usually the tracer diameter is about $\leq 1\%$ of the depth of the measurement volume. To excite fluorescent particles a laser or a LED is used. We present an adapted APTV procedure, which is based on the ball lens effect of transparent, non-fluorescent particles. We focus on measurement situations where particles images cover up to $\sim 3\%$ of the field of view. This is significantly larger than in conventional APTV, where particles cover around $\sim 10^{-5}\%$ to $10^{-4}\%$ of the field of view.

2 Experimental Setup

The measurement system consists of a microscope (Nikon Eclipse LV100) with a continuous backlight illumination. For image-recording, two cameras were used for a comparative study. These are a 12-bit, CMOS high-speed camera (Phantom Miro Lab 110, Vision Research) with $20\mu\text{m}$ pixel size, as well as a 12-bit, dual frame, CCD-camera (Imager ProSX, LaVision GmbH) with a pixel size of $5\mu\text{m}$. A schematic drawing and a picture of the full experimental setup are shown in Figs. 1a and b, respectively. Measurements are performed with two Nikon Cfi60 objective lenses of $M=20$ and $M=10$ magnification. To introduce astigmatism, a cylindrical lens with a focal length of $F_L=200\text{mm}$ is placed in front of the CCD-chip.

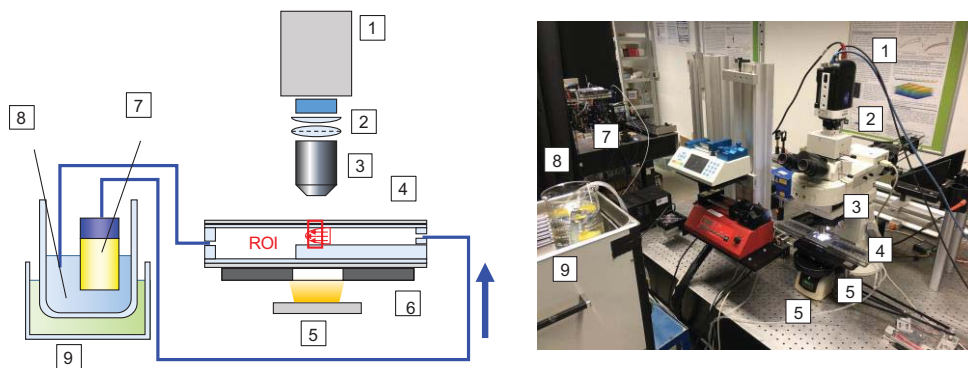


Figure 1: a) Schematic sketch of the experimental setup. b) Picture of the experimental setup in the laboratory. 1) High speed camera 2) Cylindrical lens and field lens 3) Microscope objective 4) Transparent channel 5) Backlight illumination 6) x,y,z-stage 7) Submerged pump 8) Glycerol-water solution 9) Cooling tank

3 Principle of BLAPTV

Transparent particles are illuminated in bright field mode. Due to the refractive index jump between particles and liquid, the particles act as ball lenses and focus the light into a bright focal point at some distance between particle and objective as illustrated in Figs. 2a and b. A cylindrical lens in front of the CCD-chip, creates a distorted image of the particle focal point in the image plane, henceforth referred to as "focal image". The shape of the focal image changes based on the z-location of the focal point in the object plane with respect to the focal planes

F_{xz} and F_{yz} . Three exemplary focal point positions are illustrated in the x-z and x-y plane in Figs. 2a and b. When the focal point is located in the middle between both focal planes, the focal image appears circular and stretches to a vertically or horizontally aligned ellipsoid when the focal point is located closer to F_{xz} and F_{yz} , respectively. The ratio of the ellipsoid's major and minor axes a_x and a_y , will be hereafter referred to as aspect ratio $a = \max(a_x, a_y) / \min(a_x, a_y)$. Hence, when a_x and a_y are known, the location of the focal point can be reconstructed using different calibration approaches, see Rossi and Kähler 2014. In addition to conventional APTV, for reconstructing the particle's position, the distance between the particle and its focal point needs to be determined. We call this distance the particle's apparent focal lengths, denoted as ΔF_{xz} and ΔF_{yz} (see Fig. 2c-e). The apparent focal lengths ΔF_{xz} and ΔF_{yz} can be determined as the difference of the z-coordinates where a particle itself is focused relative to the location where the aspect ratio of the focal image is one ($a=1$) (see Figs. 2c-e). Either ΔF_{xz} or ΔF_{yz} can be used consistently to reconstruct particle out-of-plane positions.

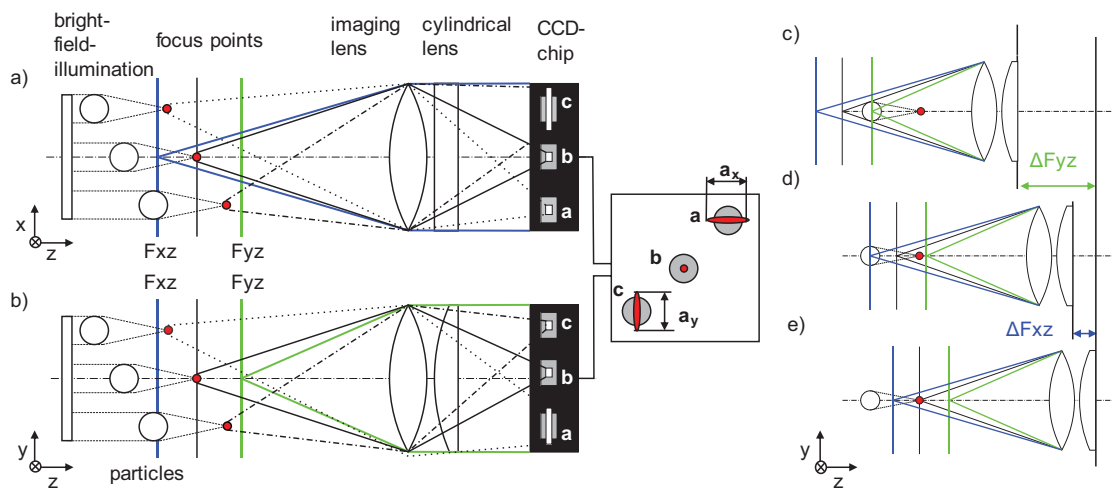


Figure 2: a) and b) Illustration of three out-of-plane focal point positions and corresponding focal images in BLAPTV. c-e) Indicating the apparent focal lengths: ΔF_{yz} and ΔF_{xz} at three specific traversing stages during calibration measurements. c) Particle rim is located in F_{yz} . d) Particle rim is located in F_{xz} . e) The particle's focal point is located in the center between focal planes and appears round in the image plane.

4. Calibration measurement

To determine the apparent focal lengths ΔF_{xz} and ΔF_{yz} and the change of the focal image axes a_x and a_y , wall-attached particles are scanned in out-of-plane direction along the z-axis in $1\mu\text{m}$ steps. In this way the shape change of the focal image as well as the focusing and defocusing of the particle itself is captured. Fig. 3a shows the evolution of the corresponding focal image of a $60\mu\text{m}$ PMMA particle with $M=20$ magnification in a 25%wt glycerol-water solution. The z-position where $a(z)$ equals one is taken as reference position, referred to as z_0 such that $a(z=z_0)=1$. To measure ΔF_{xz} and ΔF_{yz} the Tenengrad variance f is computed according to Pertuz et al. 2013, in four regions of interest (ROI) at the edge of a particle image (see Figs. 3b,c). This yields two Tenengrad variances f_{yz} and f_{xz} . When $f_{yz}(z-z_0)$ or $f_{xz}(z-z_0)$ reaches a peak value, the particle rim is focused in F_{xz} or F_{yz} , respectively. The change of a_x , a_y and their ratio a are determined from preprocessed images with an autocorrelation method as indicated in Figs. 3d-g. This procedure was found to be insensitive to light intensity fluctuations (see Cierpka et al. 2010). First, the image of the detected particle (Fig. 3d) is cropped out by the particle radius (see Fig. 3e). Hence, an autocorrelation is applied to the image section and the

aspect ratio a of the auto-correlation peak is determined by extracting isocontours at a fixed threshold (Fig. 3g). This threshold will hereafter be referred to as autocorrelation threshold c_a .

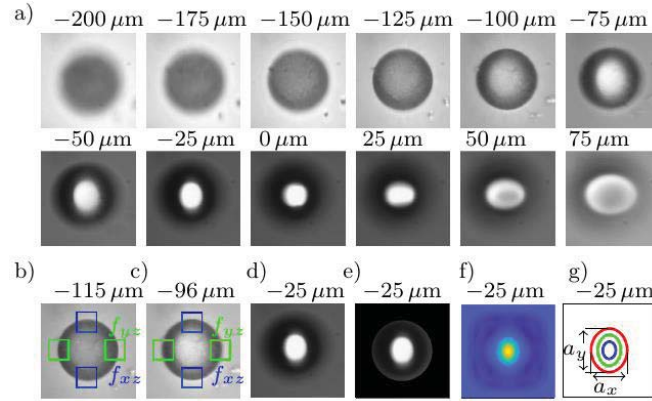


Figure 3: a) Particle images for different $z-z_0$ ($d_p=60\mu\text{m}$, PMMA). b, c) ROI to measure the focus measure f_{xz} . b) Particle is focused in F_{yz} . c) Particle is focused in F_{xz} . d) Raw particle image. e) Preprocessed particle image. f) Autocorrelation map of Fig. 3e. g) Autocorrelation iso-contours red: $c_a=0.7$, green: $c_a=0.4$, blue: $c_a=0.155$).

To illustrate the calibration procedure, a $60\mu\text{m}$ PMMA particle is suspended in water and scanned along the z -axis at $M=20$. From these image series the major and minor axes length a_x and a_y as well as their aspect ratio a and the Tenengrad variances f_{xy} and f_{xz} are extracted and plotted as functions of the relative z -position $z-z_0$ in Fig. 4a. As described earlier, two focal planes F_{xz} and F_{yz} coexist in the system due to the presence of a cylindrical lens in the optical path. F_{yz} is located closer to the camera compared to F_{xz} . As a consequence ΔF_{xz} is smaller than ΔF_{yz} (see Fig. 4a). When the focal planes are traversed along the z -axis (corresponding to increasing $z-z_0$ values), the focal image transforms from a vertically aligned ellipsoid ($a_y > a_x$ for $z-z_0 < 0$) to a horizontally aligned ellipsoid ($a_y < a_x$ for $z-z_0 > 0$). As a result, the aspect ratio a (black curve in Fig. 4a) shows a characteristic M-shape.

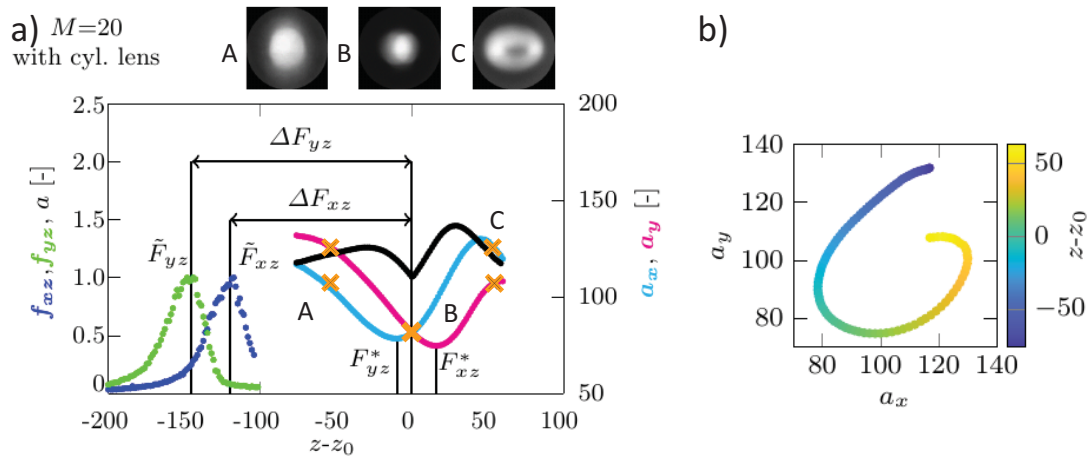


Figure 4: Calibration measurement for a $d_p=60\mu\text{m}$ PMMA particle in water ($c_a=0.4095$, $c_i=0.77$). a) Evolution of normalized Tenengrad variances f_{yz} (green), f_{xz} (blue), focal image axes lengths a_x (cyan), a_y (magenta) and their aspect ratio a (black). b) Calibration curve with a_y plotted as function of a_x .

The focal image appears circular in the image plane when the focal point is located at center between both focal planes F_{yx} and F_{zx} , that is when $a_y=a_x$ for $z-z_0=0$ (see Fig. 4a). In this situation the focal image appears round but slightly blurred. The distance of the focal planes

$F_{yx}-F_{zx}$ can be determined from Fig. 4a. $F_{yx}-F_{zx}$ is equal to the distance $\tilde{F}_{xz}-\tilde{F}_{yz}$, at which the particle itself is focused in F_{yx} , F_{zx} , as well as to the distance $F_{xz}^*-F_{yz}^*$ where the focal point is focused in F_{yx} , F_{zx} (see Fig. 4a). When a_y is plotted over a_x we obtain a characteristic calibration curve as shown in Fig. 4b, where each pair of a_x , a_y is associated with the corresponding $z-z_0$ position of the focal point as indicated by the color bar.

5 Generating a calibration function

The major steps to generate a calibration function are illustrated in Figs. 5 a-c. In the first step a set of particles located at the channel bottom is scanned to gain a set of independent data for $a_x(z-z_0)$, $a_y(z-z_0)$ and $I(z-z_0)$ (see Fig. 5a). Hence, a median curve $I(z-z_0)$ of all I scatter data is generated. Its maximum is denoted as I_{\max} (see Fig. 5a). The measurement volume depth over which out-of-plane focal image reconstructions are performed, is determined through the z -range for which $I(z-z_0)$ fulfills the following condition: $I(z-z_0) > c_I \cdot I_{\max}$. The pre-factor, referred to as intensity coefficient c_I is set to 0.65 for the case presented in Fig. 5. Next, polynomials of 7th order are fitted to the relevant $a_x(z-z_0)$ and $a_y(z-z_0)$ scatter data (see Fig. 5b). The actual calibration function is composed of the resulting curve $a_y(a_x(z-z_0))$ as shown in black in Fig. 5c. With this data in hand, we can reconstruct the $z-z_0$ position of the focal image of a particle in the flow by determining the Euclidean distance of single data points onto the calibration curve and hence the corresponding $z-z_0$ position (Cierpka et al. 2011). A data point is considered as valid if it stays within a certain Euclidean distance. Otherwise, it is rejected (see red dots in Fig. 5c). For the given case the measurement range is $z-z_0=125\mu\text{m}$ with a position reconstruction error of $\sigma_z=1.32\mu\text{m}$, for the position of the focal point. It may be noted, that the error for the position of the particle is higher, due to the error in determining ΔF_{yx} or ΔF_{xx} .

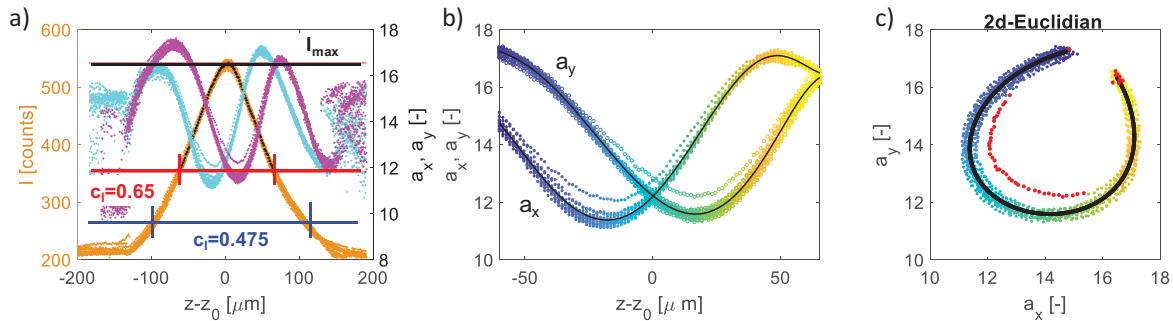


Figure 5: Procedure of generating a calibration function ($c_a=0.7311$, $c_I=0.65$). a) Selecting range ($z-z_0$) of scattered data based on the light intensity I . Symbols: orange= I , black=median of I , magenta= a_y , cyan= a_x . b) Polynomial fit (black curve) to scatter a_x , a_y . c) Resulting calibration curve (black curve) and scattered data of a_x , a_y in the a_x - a_y space with rejected data points (red).

If c_I is decreased, for example from $c_I=0.65$ to $c_I=0.475$ for the given case, the measurement range increases from $z-z_0=125\mu\text{m}$ to $z-z_0=211\mu\text{m}$ as indicated by the vertical red and blue bars in Fig. 5a. However, increasing the $z-z_0$ range may lead to intersections of the calibration curve in the a_x - a_y space as shown in Fig. 6a. These intersections cause ambiguities and lead to large errors. We overcome this issue by extending the a_x - a_y -calibration curve to the a_x - a_y - I space (see Fig. 6b). Analogous to the a_x - a_y -calibration curve, data points too far away from the a_x - a_y - I -calibration curve are rejected, as indicated by the red dots in Fig. 6b. In Fig. 6c, the calculated $z-z_0$ obtained by the 2d- and 3d-Euclidian calibration curve is plotted over $z-z_0$ reference values. As can be seen, the averaged error is significantly higher for the 2d-

Euclidian curve ($\sigma_z=30.43\mu\text{m}$) than for the 3d-Euclidian curve ($\sigma_z=1.20\mu\text{m}$), due to ambiguities visible in Fig. 6a (highlighted with a red ellipsoid). These ambiguities lead to large deviations highlighted in Fig. 6c (red ellipsoids).

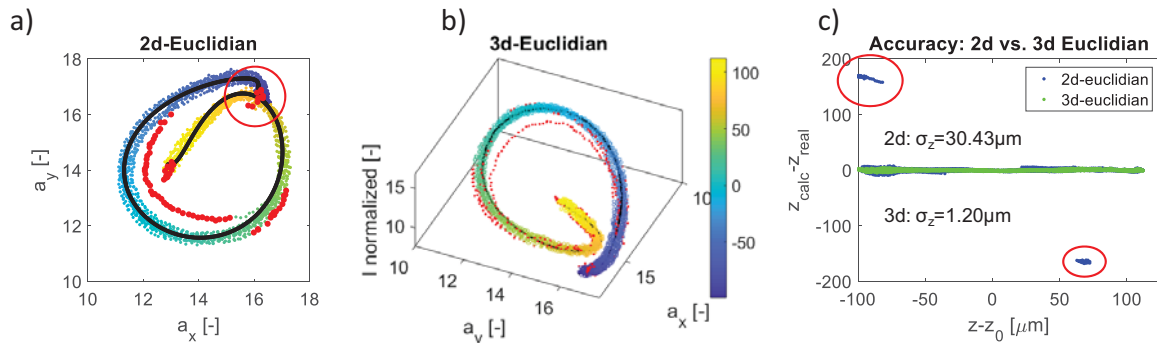


Figure 6: a) 2d-Euclidian calibration curve showing intersections ($c_a=0.7311$, $c_i=0.475$). b) 3d-Euclidian calibration curve in the a_x - a_y - I space without intersections. c) Comparison of the accuracy obtained from a 2d- and 3d-Euclidian calibration curve.

6 Parametric study

Fig. 7a shows the influence of the particle size on the shape of corresponding calibration curves for PMMA particles in a 25wt% glycerol-water solution. Overall, a_x and a_y values increase with increasing particle diameter d_p . In fact, calibration curves are strongly shifted without any overlap region. Hence, by assigning particles to one of these calibration curves, it is possible to determine both the out of plane position and size of a particle from a measurement. The effect of the refractive index jump between liquid and particle is shown in Figs. 7b and c. In Fig. 7b a change in refractive index jump is realized by different water glycerol mixtures resulting in different refractive indices of the liquid (n_L). Fig. 7c shows how the calibration curve is affected by particles of different refractive index (n_P). With decreasing $n_P - n_L$ the overall size of the focal image increases, resulting in rising a_x and a_y values, such that the calibration curves are shifted. From Fig. 7c we conclude that it is possible to determine the particle's out-of-plane position and to identify a particle's material through its refractive index at the same time, by assigning it to a calibration curve. This may be a useful instrument to investigate suspensions of particles of different materials or sizes.

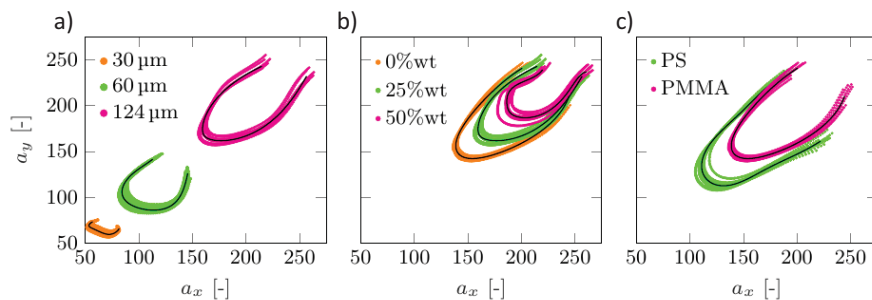


Figure 7: Influence of experimental parameters on calibration curves ($c_a=0.4095$, $c_i=0.77$). a) Influence of particle size (PMMA, 25%wt glycerol). b) Influence of refractive index jump (refractive index of liquid varied, PMMA, $d_p=124\mu\text{m}$). c) Influence of refractive index jump (refractive index of particle n_P varied, $d_p=124$, 0%wt).

7 Validation measurement

To demonstrate the capability of the measurement technique for flows beyond sub-millimeter measurement volume depths, we validate the measurement technique with a plane channel flow of 2305 μm channel height. The liquid was seeded with polystyrene particles of $d_p=80\mu\text{m}$, being two orders of magnitude smaller than the channel height. A 25wt% glycerol and 75wt% deionized water solution was used for the measurements to achieve a density matching to the particles. The liquid was seeded with $10^{-4}\text{wt}\%$ particles. To determine the absolute position of the channel walls prior to the experiments, the whole channel gap is scanned in steps of $1\mu\text{m}$ in resting fluid with particles drifted to the top or the bottom wall within the field of view. Typically, 20 particles located at the top and bottom wall of the channel are included in the calibration procedure. The resulting calibration curves and the associated scattered a_x and a_y -values are presented in Fig. 9a. Obviously, the calibration curve for particles located at the top wall ($z=2305\mu\text{m}$) differs from those of particles located at the bottom wall ($z=0\mu\text{m}$). We anticipate, this is due to the different distance the light of the focal point has to travel through the liquid until it reaches the image plane. Furthermore, ΔF_{xz} and ΔF_{yz} differ for particles located at the top wall or at the bottom wall (see Tab 1.)

| | $z=0\mu\text{m}$ | $z=2305\mu\text{m}$ | Δ |
|-----------------|------------------------------|-----------------------------|--------------------|
| ΔF_{xz} | $175.62\pm 8.33\mu\text{m}$ | $143.28\pm 8.83\mu\text{m}$ | $32.34\mu\text{m}$ |
| ΔF_{yz} | $203.84\pm 12.86\mu\text{m}$ | $166.87\pm 9.91\mu\text{m}$ | $36.97\mu\text{m}$ |

Table 1: Measured particle apparent focal length ΔF_{xz} and ΔF_{yz} for $z=0\mu\text{m}$ and $z=2305\mu\text{m}$.

Due to the different shape of the calibration curves, the challenge is to find a calibration function that is valid for particles located at any z -position in between the bottom and top channel wall. To overcome this problem, we linearly interpolate a_x and a_y of the calibration curves as a linear function of z . Also, the calibration parameters, ΔF_{xz} , ΔF_{yz} , I_{\max} are fitted linearly. In Fig. 8b 50 linear fits at locations evenly distributed between $z=2305\mu\text{m}$ and $z=0\mu\text{m}$ are displayed.

After the calibration measurement, a volume flow rate of $3.75 \times 10^{-4} \text{ m}^3/\text{s}$ was created using a submerged rotary pump. The mass flow rate was calculated based on the density of the glycerol-water mixture Cheng et al. 2008. The liquid was continuously recirculated and its temperature was constantly kept at $19\text{-}20^\circ\text{C}$ with a cooled water tank. After starting the pump, we waited for two hours to ensure that the system reaches a steady temperature. Hereafter, the gap was scanned in steps of $136\mu\text{m}$ with 5300 pictures of 520×460 pixel resolution recorded at 1000fps at each measurement plane. After the flow measurement, all calibration curves displayed in Fig. 8b, are compared to the measured a_x and a_y data of each measurement plane. The interpolated calibration that provides the most valid pairs of a_x and a_y in terms of Euclidian distance is considered as a match and selected for determining the $z-z_0$ of the a_x and a_y pairs in the respective measurement plane. Instead of using a light intensity calibration curve as described in section 5 we use a simplified intensity criterion: Data with $I < I_{\max} \cdot c_l$ is rejected. In Fig. 8b the best matching calibration curve for the measurement plane at $z=1115\mu\text{m}$ is plotted. Likewise, the values of ΔF_{xz} , ΔF_{yz} , c_l corresponding to these best fitting curves are selected for the computation of the particle focal point and hence particle positions with respect to the measurement plane. Fig. 8c shows the velocity profile obtained with the previously described evaluation procedure that is performed for each measurement plane. The experimental velocity profile shows a good agreement with the analytical Poiseuille profile. The mean standard deviation of u_x along z was about $\sigma_u=0.87\%$ of the maximum velocity u_{\max} . For the out-of-plane component u_z the standard deviation assumes $\sigma_w=4.87\%$ of the maximum velocity u_{\max} , whereas the mean standard deviation for u_y is found to be $\sigma_v=1\%$. These values

are comparable to uncertainties reported by Cierpka et al. 2011 with $\sigma_u=0.9\%$ and $\sigma_w=3.72\%$ of u_{\max} for APTV based on fluorescent microparticles.

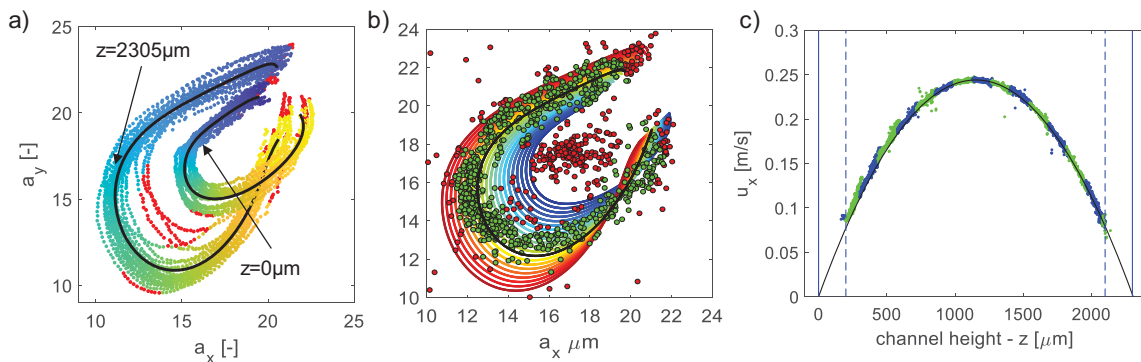


Figure 8: a) Calibration curves for particles located at $z=0\mu\text{m}$ or $z=2305\mu\text{m}$. ($c_i=0.6$, $c_a=0.7$) b) Interpolated calibration curves (colored lines). Black line=Best matching calibration curve for the measurement plane at $z=1517\mu\text{m}$. Scattered data= a_x and a_y for the measurement plane at $z=1517\mu\text{m}$, red=rejected, green=accepted. c) Experimental (green and blue dots=scattered data for different measurement planes) vs. analytical velocity profile (black line). Solid blue lines=channel wall.

9 Conclusion and Outlook

In the present study, a calibration procedure for Ball Lens Astigmatism Particle Tracking Velocimetry (BLAPTV) is presented achieving out-of-plane reconstruction accuracies for the focus point of microparticles in the order of 4% of the particle diameter. We show that the robustness, accuracy and measurement volume thickness can be increased if the Euclidian calibration method is extended to calibration curves in a_x - a_y - z space. In addition, the influence of particle size and refractive index jump on the calibration curve shape is investigated. We conclude that particles of different size and material can be identified by assigning them to different, in the a_y - a_x domain spatially separated calibration curves. Furthermore, a methodology is established to account for shape changes of the calibration curve along the measurement volume depth. Finally, the measurement technique is validated for a plane Poiseuille flow showing a good agreement with the corresponding analytical velocity profile.

Literature

- Kao, H. P., & Verkman, A. S. 1994.** Tracking of single fluorescent particles in three dimensions: use of cylindrical optics to encode particle position. *Biophysical journal*, 67(3), 1291-1300.
- Ragan, T., et al. 2006** 3D particle tracking on a two-photon microscope. *Journal of fluorescence*, 16(3)
- Cheng, N. S. 2009.** Formula for the viscosity of a glycerol-water mixture. *Industrial & engineering chemistry research*, 47(9), 3285-3288.
- Chen, S. et al. 2009.** Wavefront sensing for three-component three-dimensional flow velocimetry in microfluidics. *Experiments in Fluids*, 47(4-5), 849.
- Cierpka, C., et al., 2010:** "A simple single camera 3C3D velocity measurement technique without errors due to depth of correlation and spatial averaging for microfluidics." *Meas. Scie.* 21.4 (2010)
- Cierpka, C., et al., 2011:** "On the calibration of astigmatism particle tracking velocimetry for microflows." *Measurement Science and Technology* 22.1 (2010): 015401.
- Cierpka, C., & Kähler, C. J. 2012.** Particle imaging techniques for volumetric three-component (3D3C) velocity measurements in microfluidics. *Journal of visualization*, 15(1), 1-31.
- Pertuz, S., et al. 2013.** Analysis of focus measure operators for shape-from-focus. *Pattern Recognition*
- Buchmann, N. A. et al. 2014.** Ultra-high-speed 3D astigmatic particle tracking velocimetry: application to particle-laden supersonic impinging jets. *Experiments in fluids*, 55(11), 1842.
- Rossi, M., & Kähler, C. J. 2014.** Optimization of astigmatic particle tracking velocimeters. *Experiments in fluids*, 55(9), 1809.